scientific reports

Check for updates

OPEN

Hydrothermally synthesized VS_2/MoS_2 nanocomposites with better optoelectronic and antimicrobial response

B. Dandasena[1], S. Das[1], A. Parida[1], R. Praharaj[2], S. K. Samal[2], C. Sripan[3] & R. Naik[1]✉

Transition metal dichalcogenides (TMDs) in their 2D form have potential applications in optoelectronics and biomedical applications. The current study focuses on the synthesis of VS_2/MoS_2 nanocomposite by one-pot hydrothermal method with varying molybdenum (Mo) concentrations and investigating its superior antimicrobial activity and optoelectronic responses. The existence of both VS_2 and VS_2/MoS_2 hexagonal phases was revealed from X-ray diffraction study, which is well supported by the high-resolution transmission electron microscopy (HRTEM) study that confirms the formation of a VS_2/MoS_2 composite showing the presence of both VS_2 and MoS_2 planes. The crystallite size decreased with an increase in Mo content. The nanosheet-like structure of VS_2 and a flower-like structure of VS_2/MoS_2 were confirmed by field emission scanning electron microscopy (FESEM) imaging. The existence of V-S and Mo-S vibrational modes was evident from Raman analysis. The optical band gap value of the material increased with the increased amount of molybdenum concentration. This made them tunable for various optoelectronic applications. The oxidation states of different elements were probed through X-ray photoelectron spectroscopy (XPS). The antimicrobial study done using the disk diffusion method on gram-positive and negative bacteria revealed better antimicrobial efficacy on gram-negative bacteria than on gram-positive bacteria. The observed changes in its optical, morphological, and structural properties are suitable for optoelectronic applications, whereas the superior antimicrobial response is suitable for biomedical applications.

Keywords Hydrothermal synthesis, VS_2/MoS_2, Nanoflower, Nanosheet, Tunable band gap, Anti-microbial activity

TMDs are layered materials, similar to graphene, in which the transition metal atomic layer is sandwiched between two layers of the chalcogenide, bonded together by weak Van der Wall forces, which are strong in-plane bonding and weak out-of-plane bonding[1].VS_2 and MoS_2 are two different kinds of TMDs; V is the group 5th element of the periodic table, and Mo is the group 6th element. Their electronic configuration is [Ar] $3d^3$ $4s^2$ and [Kr] $4d^5$ $5s^1$, respectively, and for sulfur, it is [Ne] $3s^2$ $3p^4$. TMDs have different stacking sequences, namely 1T, 2H, and 3R for trigonal, hexagonal, and rhombohedral, respectively. Among them, the 1T and 2H polytypes of VS_2 and MoS_2 are thermodynamically stable phases. The distinct electronic properties of metallic and semiconducting MoS_2 arise from their different electron configurations, with the metallic phase exhibiting partially filled valence bands, while the semiconducting phase has fully filled valence bands. Although the 1T and 2H phases share a similar crystal structure, these differences in electronic arrangements may influence their relative stability due to variation in electronic energy. For instance, the 1T phases of MoS_2 have formation energies that are 0.84 eV, and 0.55 eV per formula unit higher than those of the 2H phase. Due to the lowest free energy, the phases are thermodynamically stable[2,3].The 1T poly-type of VS_2 is known for its different optical and electronic properties. The hexagonal structure is the most common form of VS_2 [4].Due to the variable bandgap properties, TMDs are very useful in optoelectronic applications[5–11].Apart from other applications, these TMDs also show good antimicrobial activity, which leads to biomedical applications[12].The high surface-to-volume ratio of 2D material is beneficial for different biomedical applications, including biosensing[13],drug delivery[14,15],

[1]Department of Engineering and Materials Physics, ICT-IOC, Bhubaneswar 751013, India. [2]Laboratory of Biomaterial and Regenerative Medicine for Advanced Therapies, ICMR-RMRC, Bhubaneswar 751023, India. [3]Department of Physics, Dayananda Sagar Academy of Technology and Management, Udayapura, Bangalore 560082, India. ✉email: ramakanta.naik@gmail.com

photothermal therapy[16],bioimaging[17,18], and antibacterial applications. According to a previous report, the antibacterial activity of chemically exfoliated MoS_2 sheets was evaluated using the colony counting method. When E. coli DH5a was incubated for two hours with 80 mg mL^{-1}, only 40% of bacteria were killed by raw MoS_2, and 90% were killed by chemically exfoliated MoS_2[19].The incorporation of $MoSe_2$ with H_2O_2 enhances the antibacterial activity compared to H_2O_2 alone. This enhanced effect is particularly evident against Escherichia coli (*E. coli)*, and *Bacillus subtilis (B. subtilis)*. The $MoSe_2$-based films exhibit strong resistance to bacterial infection, which can be attributed to their intrinsic peroxidase-like activity[20].The antibacterial activity of MoS_2, WS_2, and $MoSe_2$ with their IT phases was tested against gram-negative E. coli bacteria. TMDs were Prepared for this activity by chemical exfoliation and the antibacterial activity by colony counting method[21]. Doping is also a good approach to improve antibacterial activity because it enhances the active surface area. Nitrogen-doped MoS_2 and WS_2, which is sowing improved peroxidase-like catalytic activity by producing more toxic OH by catalyzing H_2O_2. It is able to fight more efficiently against E. coli and B. subtilis bacteria than non-doping MoS_2 and WS_2. Here, the material was prepared using the hydrothermal method followed by ultrasonic exfoliation[22]. WX_2(X = S, Se) is exfoliated using single-standard DNA and shows antibacterial activity against *Escherichia coli* K-12 MG1655 in phosphate-buffered saline[23]. Bismuth-doped MoS_2 prepared by hydrothermal method shows increased antimicrobial response against S. aureus and E. coli bacteria[24]. Fe_3O_4@MoS_2-Ag enzyme with a rough defect-rich surface was created using in-situ photo deposition of Ag nanoparticles and a straightforward hydrothermal process. By releasing Ag + and producing reactive oxygen species, the enzyme demonstrated strong antibacterial activity against *E. coli* (~ 69.4%). Additionally, the nano enzyme could attain exceptional synergistic disinfection (~ 100%) when combined with the near-infrared photothermal characteristic of Fe_3O_4@MoS_2-Ag[25]. Zr-doped MoS_2 nano catalyst synthesized by the hydrothermal method enhances the antibacterial activity against both bacteria[26]. Hydrothermally synthesized Ce-MoS_2/WO_3 shows exceptional antibacterial activity in visible light. The antibacterial rate against *E. coli* increased to 97.8% when compared with MoS_2/WO_3(62.8%) and pure MoS_2. (44.1%). Therefore, for quick sterilization, the composite's enzyme-like catalytic activity and photodynamic effect are enhanced by the synergetic reaction of Ce-doped WO_3 and MoS_2[27]. TMDs like VS_2 and MoS_2 can generate reactive oxygen species upon light exposure or in the presence of certain catalysts. Previously, the antibacterial activity of VS_2/MoS_2 was also studied, and the antibacterial efficacy against both gram- and gram-positive bacteria was also studied[28]. CoS_2/MoS_2 shows remarkable antibacterial performance with good enzymatic and photocatalytic properties. CoS_2/MoS_2 nanosheets exhibit remarkable enzyme-mimicking capabilities in neutral media, addressing the significant limitation that nanozymes typically function only in acidic environments[29]. Several other features of the VS_2 and MoS_2 nanocomposites make them suitable for the treatment of cancerous cells. The sharp edges[30] of VS_2 and MoS_2 nanosheets can physically puncture and disrupt microbial cell membranes, resulting in eventual cell death by leakage of cellular contents. These materials can release metal ions (V^{5+} from VS_2 and Mo^{6+} from MoS_2) that have toxic effects on microorganisms. These ions can interfere with essential cellular processes and enzymes, leading to microbial death. MoS_2 is an exceptional member of transition metal dichalcogenides (TMDs) due to its expansive surface area, strong near-infrared (NIR) absorption, high biocompatibility, and low toxicity toward cells. MoS_2-based nanomaterials have displayed efficacy in inhibiting bacterial growth across various systems[31]. Premeditated the antimicrobial efficiency of CAU-17/MoS2 against both gram-negative (*E. coli*) and gram-positive (*S. aureus*) as well as Methicillin Resistant S. aureus (MRSA) and established a result which shows it has an impressive antibacterial efficacy against the test micro-organisms due to its photocatalytic properties. VS_4/Ag_2WO_4 nanocomposites were synthesized using straightforward co-precipitation and ultrasonic-assisted techniques. These nanocomposites demonstrated significant antimicrobial response against both gram-negative E-coli and gram-positive Bacillussubtilis[32]. The nanocomposite of MoS_2 and chitosan was evaluated and found to be successfully constraining the growth of both *E. coli* and *S. aureus* along with breast cancer cells, i.e., MCF7[33]. These findings underscore the nanocomposites' substantial potential as highly effective photo-catalysts for water pollutant removal and as potent antimicrobial agents. The newly synthesized nanocomposite can also be used in the biomedical field as a novel antibacterial agent against different bacterial diseases.

In the present report, the VS_2/MoS_2 nanocomposites are prepared through the one-pot hydrothermal method by varying Mo concentration. Structural investigation by XRD confirms the presence of both VS_2 and MoS_2 phases. The UV-Vis analysis infers the absorption shift resulting in the bandgap change with Mo content. The morphological images were taken using FESEM, which shows the nanoflower-like structure. The compositional study reveals the presence of constituent elements in the samples. XPS study of the material presents the details regarding the oxidation states of the different elements. The antimicrobial activity was performed on gram-positive bacteria (ATCC 25923, *Staphylococcus aureus* and gram-negative (ATCC 25922, *Escherichia coli*). It was observed that there was a very good response of anti-microbial activity against gram-negative bacteria.

Experimental procedures

Materials

Ammonium molybdate tetrahydrate $(NH_4)_6Mo_7O_{24}$. $4H_2O$,99.3%, Loba Chemie), Ammonium metavanadate (NH_4VO_3, 99%, GLR Innovations), Thioacetamide (C_2H_5NS, Thiourea (CH_4N_2S,99%, Loba Chemie), Spectrochem), Oxalic acid dehydrate($(COOH)_2.2H_2O$,99.5%, SRL Chemicals), Polyvinyl pyrrolidone K30 L R((C_6H_9NO) n, SDFCL) (PVP), Ammonia soln. Abt. 30%. (NH_3, SDFCL), all the chemicals were used directly without any modification. The solvent used is deionized water; deionized (DI) water and ethanol were used for the removal of unreacted precursors and impurities to extract the required nanoparticle.

Methods

VS_2 nanosheet preparation

A facile hydrothermal synthesis method was used to prepare VS_2 nanosheets. In a beaker containing 75 mL DI water and 5 mL ammonium hydroxide solution,2.5 g PVP, 0.585 g NH_4VO_3, and 3.755 g C_2H_5NS were added one after another, respectively. The solution is stirred for 2 h at 900 rpm at ambient temperature to make it a homogeneous solution. The solution color gradually changes from light yellow to deep brown and finally black. Then, the prepared solution was put inside a 100 mL stainless-steel autoclave (Teflon-lined). The heating was done for 24 h at 200 °C. After that, the autoclave was allowed to cool naturally. The powder was obtained after centrifugation several times by DI water and ethanol. Then, it was vacuum dried for 24 h at 60 °C. The dried sample was finely grinded with mortar pastel to obtain the VS_2 nanosheets. Scheme 1 represents the schematic of the preparation of the VS_2 nanosheet.

VS_2/MoS_2 nanocomposite preparation

First, 0.2 g of prepared VS_2 powder was taken and mixed with 40 mL of DI water in a beaker. Then, the solution was ultrasonicated in ice water for 30 min to prevent oxidation[34]. At the same time, another beaker was taken, added with 30 mL of DI water and 0.3 g of $(NH_4)_6Mo_7O_{24}\cdot 4H_2O$, and 0.8 g of CH_4N_2S. Finally, 0.4 g of oxalic acid was used for regulating pH. Then stirring of the mixture was done for 30 min at 900 rpm at normal temperature. Next, the mixing of both solutions was carried out with a stirring for 2 h to make it a homogeneous one. Then, the solution was put inside a 100 mL stainless steel autoclave (Teflon–lined). The heating was done for 24 h at 200 °C in a hot air oven. It was allowed to cool automatically. By the same cleaning process as like VS_2 nanosheet, the VS_2/MoS_2-1 nanocomposite powder was obtained. A schematic diagram is shown in Scheme 2. By varying the concentration of molybdenum precursor (0.5 g (5.7797 mmol) and 0.7 g (8.0915 mmol), another two composites are prepared, namely VS_2/MoS_2-2 and VS_2/MoS_2-3, respectively. These names are denoted throughout the paper.

Impact of PVP on nanoparticle synthesis

The role of PVP in nanoparticle synthesis varies with the specific material system and reaction conditions, where it can act as a reducing agent, growth regulator, surface stabilizer, and dispersant. By coordinating with small ions, PVP restricts nanoparticle growth, enabling the formation of ultra-small particle sizes[35]. Widely employed in nanoparticle synthesis, PVP is a nonionic, biocompatible polymer composed of C = O, C–N, and CH_2 functional groups. Its molecular structure contains both a hydrophilic pyrrolidone moiety and a hydrophobic alkyl group. Due to the highly polar amide group in the pyrrolidone ring, along with methylene and methine groups in the ring and backbone, PVP is soluble in water as well as in many nonaqueous solvents. The steric hindrance effect, arising from hydrophobic carbon chains extending into the solvent and repelling each other, makes PVP an effective stabilizer that prevents nanoparticle agglomeration[36–38]. In PVP-mediated synthesis, residual PVP may remain after the reaction. Typically, purification involves centrifugation and ethanol washing to remove excess reactants and byproducts. Nevertheless, some PVP molecules often remain bound to the nanoparticle surface, functioning as ligands and stabilizing agents. Previous studies further indicate that oxidized PVP, such as poly(vinyl(pyrrolidone)x-(succinimide)y), exhibits stronger binding affinity, which may account for its persistent association with nanoparticles[39].

Scheme 1. Preparation method of VS_2 nanomaterial.

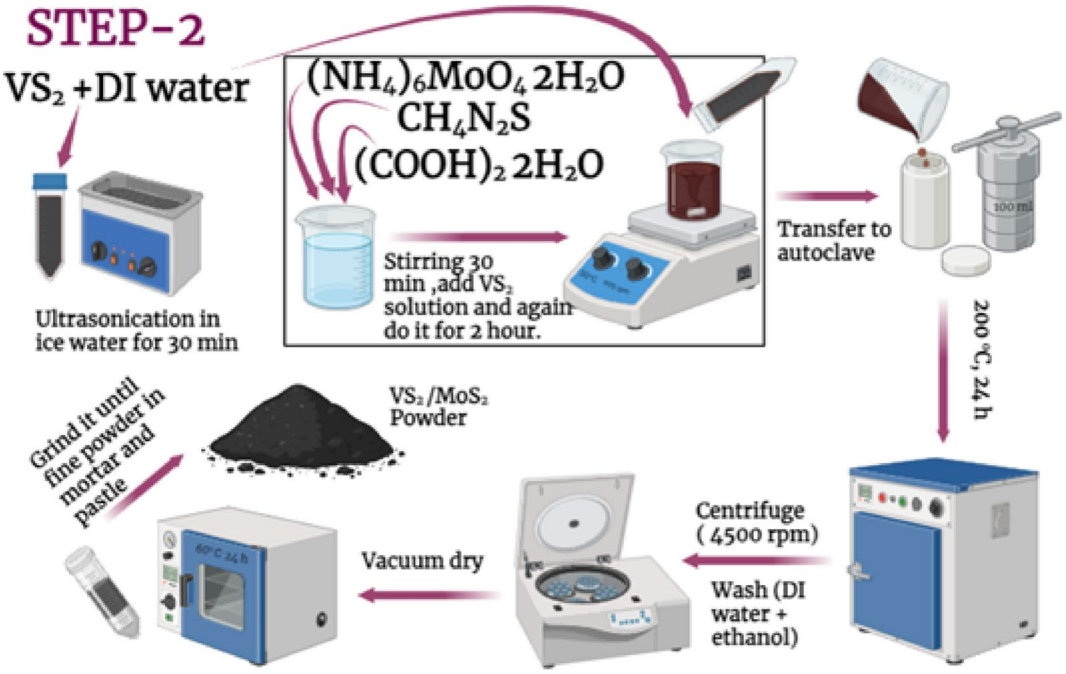

Scheme 2. Preparation method of VS_2 nanomaterial.

Characterization techniques

The powder XRD data for the samples were measured by using CuK_α radiation (λ = 1.5418 Å) source (XRD Instrument-Bruker D8 ADVANCE). The data were recorded at 30 kV and 40 mA. The data scan was done with step size 0.02° in 2θ range of 10° – 80° at a grazing angle of 1°. Raman data was recorded from the HORIBA 1024*256-OE spectrometer and a charge-coupled device (CCD) detector. The spectra were taken from 50 to 700 cm^{-1} by using a 633 nm helium-neon laser with a resolution of 0.5 nm. The morphology of the samples was assessed using FESEM (JEOL, JMS-7610 F plus) operated around 20 to 200 kV. The surface morphological view of the samples was imaged by the FESEM unit at various portions of the film with different scales. The high-resolution surface images were collected via TEM supplied by JEOL, TEM-2100 PLUS instrument. The planes present in the sample were verified from the selected area electron diffraction (SAED) pattern. The element confirmation of the samples was determined by an energy-dispersive X-ray (EDX) spectrometer. The elemental mapping for the samples showing the distribution of elements was taken through EDX. The XPS instrument (Axis Ultra Kratos Analytical, UK) was employed to study modifications in the chemical structure and compositions. Core level XPS spectra were obtained using Al K_α X-rays (1486.6 eV) under a vacuum of 2×10^{-9} Torr. The XPS data consisted of survey scans of the entire binding energy (BE) and selected scans of the core level peaks of interest. An energy increment of 1 eV was used for recording the survey spectra and 0.05 eV for the case of core level spectra. The core level peaks were recorded by sweeping the retarding field and using the constant pass energy of 30 eV. Data were averaged over three scans. The reproducibility of the measurements was checked on different regions of the investigated surfaces. For this study, adventitious carbon was used as a reference, and the BE of the reference C 1*s* line was set as 284.6 eV. The reflectance data was captured by JASCO V-770 UV-visible spectrophotometer between 200 and 1200 nm at 0.5 nm spectral resolution. The data were obtained at an interval of 1 nm.

Minimum inhibitory concentration (MIC) by broth Dilution method

In this procedure, the MIC was done to check the minimum concentration of the materials required to kill or inhibit the growth of bacteria. Here, both gram-negative (ATCC 25922, *Escherichia coli*) and gram-positive bacteria (ATCC 25923, *Staphylococcus aureus*) strains were used to perform MIC. First of all, solutions of material were prepared at a concentration of 25 mg/mL, 50 mg/mL, and 100 mg/mL by adding the appropriate amount of material in 1 mL of Dimethylformamide (DMF). MIC was performed by adding 10 µl of prepared solution of materials from each concertation to the Nutrient Broth (NB), and in that fresh culture of the standard strains of both gram-positive (*E. coli*) and gram-negative (*S. aureus*) (0.5 McFarland) was inoculated, and at last, PBS was added to maintain the volume. Then, the mixture was incubated at 37 °C for 36 h. Turbidity was observed afterward.

Disk diffusion method

Several methods have been used to evaluate antimicrobial properties[40,41]. Among all of these, the disk diffusion system is one of the most used techniques[42–45]. In order to evaluate diffusion and the antimicrobial efficacy of these newly designed materials, the disk diffusion method was used. The antibacterial response of the synthesized material (VS_2/MoS_2-3) was evaluated by using both gram-negative (ATCC 25922, *Escherichia coli*)

and gram-positive bacteria (ATCC 25923, *Staphylococcus aureus*). The pure colonies were isolated from ATCC samples by quadrant streaking. Then, fresh culture was prepared using a Nutrient Broth (NB) medium, and the bacterial concentration of 0.5 McFarland constant (1.5×10^8) was prepared. Afterward, 100 µl of fresh culture was swabbed all over the surface of the Mueller Hinton Agar (MHA) plate using a sterile cotton swab and left for drying for about 20 min. In the meantime, newly synthesized material was dissolved in Dimethylformamide (DMF) at 100 mg/mL concenmlmltration, and 6 mm sterile disks were soaked in a solution of material. Some disks were soaked in DMF (for control) for 6 h as well. Afterward, 2 disks were placed on the swabbed plate, one with only DMF as positive control and another impregnated with a material solution. Then, incubation of these plates was done at 37 °C for 24 h. The material's antimicrobial activity was observed using macroscopic images and their respective inhibition zones.

Result and discussions

XRD study

VS_2 and VS_2/MoS_2 nanocomposite XRD pattern is illustrated in Fig. 1. The prepared VS_2 nanomaterial shows a hexagonal phase (JCPDS:36-1139)[34]. Two prominent peaks of VS_2 at 15.70° and 36.50° were directed along the (001) and (101) crystallographic plane. The fingerprint of pure hexagonal MoS_2 (ICSD:01-075-1539) is also shown in Fig. 1. Three prominent peaks of MoS_2/VS_2 nanocomposite are observed at 13.93°, 33.33°, and 59.25°, which correspond to (002), (100), and (110) planes, respectively. The broader peak observed is due to the merging of pure VS_2 and MoS_2 peaks. The first (13.93°), second (33.33°), and third (59.25°) peaks of the composite are

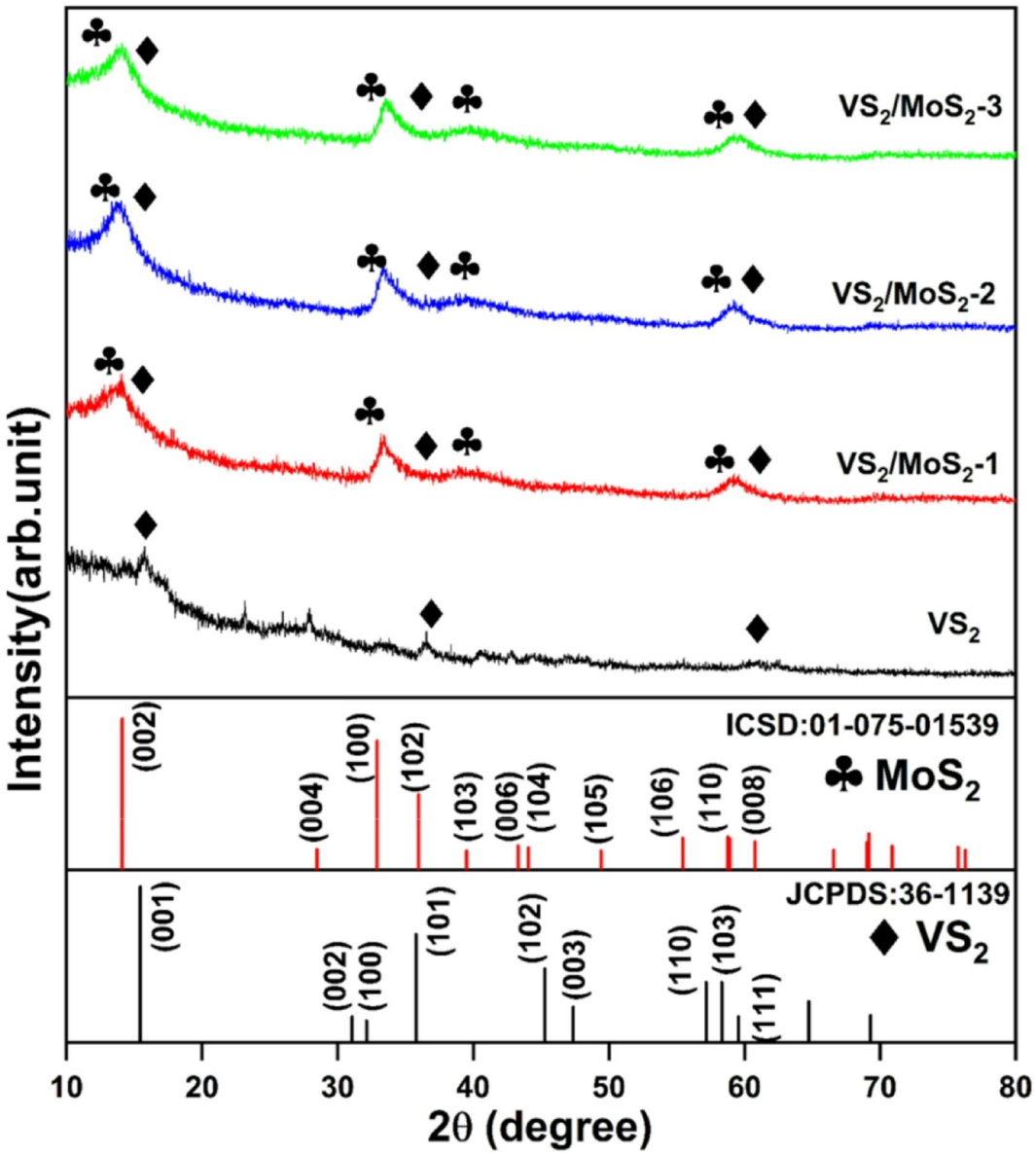

Fig. 1. XRD pattern of VS_2 and VS_2/MoS_2 nanocomposite.

due to the (001) plane of pure VS_2, (002) plane of pure MoS_2, (100) plane of pure VS_2, (101) plane of pure MoS_2 and (110) plane of pure VS_2, (111) plane of pure MoS_2 respectively[34,46,47]. MoS_2/VS_2 nanocomposite diffraction peak located at 13.93° and corresponding to the MoS_2 (002) plane is less than that of pure MoS_2(2θ = 14.4°), indicating the (002) plane's larger interlayer distance[48]. The reduction of grain size is due to the broader and weaker peak of the nanocomposite.

The X-ray diffraction data gives us valuable information such as crystalline phase, crystal structure, crystallographic orientation, crystallite size, strain and phase purity, etc[48]. Broader peaks are observed that lead to smaller crystallite sizes. Debye-Scherrer equation is used to determine the crystallite size (D) by [49],

$$\mathrm{D} = \frac{K}{\beta \cos(\theta)} \tag{1}$$

with K = 0.9 as the shape factor. λ = 1.54 Å as the CuK_α wavelength of. β as the full width at half maximum (FWHM). The calculated values are listed in Table 1 .The average crystallite size decreased with the increase in the molybdenum concentration; values are 4.6 nm,4.39 nm, and 4.29 nm, respectively. The D value of VS_2 is 13.81 nm. All calculated values are presented with their corresponding standard deviations, and the detailed calculations are provided in **Table S1**. The Dislocation density is the number of dislocation lines per unit volume of a crystal as calculated[49].

$$\text{Dislocation density } (\delta) = \frac{1}{D^2} \tag{2}$$

In nano-crystalline materials, lattice distortion, characterized by micro-strain and lattice parameter change, is commonly encountered. The fundamental explanation for the lattice distortion is thought to be the internal stress caused by the extra volume at grain boundaries[31]. The micro-strain produced inside the material is given by,[49]

$$\text{Micro} - \text{strain } (\epsilon) = \frac{\beta}{4\tan(\theta)} \tag{3}$$

Raman analysis

Raman spectra analysis was performed to verify the microstructure and insight into the details of the phonon active mode of VS_2 and VS_2/MoS_2 nanocomposite. The Raman data was taken in the 50–700 cm^{-1} range for all the prepared nanocomposites, as presented in Fig. 2. The characteristic pristine VS_2 peaks are located approximately at 192, 219, 271,286.5 and 346 cm^{-1}, which are arises due to the different rocking and stretching vibration of V-S bond vibrational modes[50,51].192 cm^{-1} and 219 cm^{-1} peaks are due to the V-S bond stretching. The peak formed at 271 cm^{-1} and 286 cm^{-1} is due to the $E_{2g}{}^1$ in-plane phonon mode arises due to the opposite vibration of two S atoms with respect to V atom[52] .

The characteristic peak of VS_2 at 192 cm^{-1} is observed in the composite sample, while the other peaks are not clearly visible. Both in-plane(E^1_{2g}) and out-of-plane (A_{1g}) vibrational mode peaks of MoS_2 located at 378.9 and 406.9 cm^{-1} are clearly observed in all three nanocomposite samples[53]. In the nanocomposite the peak appeared at 228 is due to the MoS_2[54,55]. The peak intensity gradually increased with higher molybdenum concentration. The presence of both VS_2 and MoS_2 vibrational mode peaks of Raman also confirms the formation of the composite.

FESEM and EDX analysis

The morphology of the nanomaterial is determined by FESEM images. Figure 3.a, b illustrates the FESEM pictures at different magnifications of VS_2/MoS_2-1. From the observation, it is found that the VS_2/MoS_2-1 sample morphology exhibits a flower-like structure. An essential method for examining the compositional variance in the material is elemental mapping. Figure 3. c-f shows the elemental mapping of VS_2/MoS_2-1. The material's homogeneous distribution of V, S, and Mo components confirms the successful completion of a uniform VS_2/MoS_2 nanocomposite through the elemental mapping. EDX spectra of VS_2/MoS_2-1, from Fig. 3.g, confirm the elemental presence of the prepared sample. Figure 4. represents the FESEM pictures of two other compositions, such as VS_2/MoS_2-2 and VS_2/MoS_2-3, with two different magnifications.

Fig S1a, b represents the FESEM images of VS_2 with different magnifications. Some other reports also show similar morphology[56]. An average thickness of 43 nm is found for the nanosheets. All other EDX spectra are provided in Figure S2a, b, c. Different peaks for the various elements present in the material can be seen in the EDX spectrum. 0.511 keV and 4.952 keV are the energies corresponding to the L_α and K_α transitions for the

Structural parameter	D (nm)	δ (x10^{-3} nm^{-2})	Micro-strain (ε) × 10^{-3}
VS_2	13.81 ± 7.69	12.11 ± 12.3	10.45 ± 6.16
VS_2/MoS_2-1	4.65 ± 0.69	50.13 ± 15.0	35.58 ± 22.72
VS_2/MoS_2-2	4.39 ± 0.12	57.05 ± 18.2	39.97 ± 28.97
VS_2/MoS_2-3	4.29 ± 0.83	58.08 ± 18.2	36.013 ± 9.41

Table 1. Structural parameter of VS_2 and VS_2/MoS_2 nanocomposite.

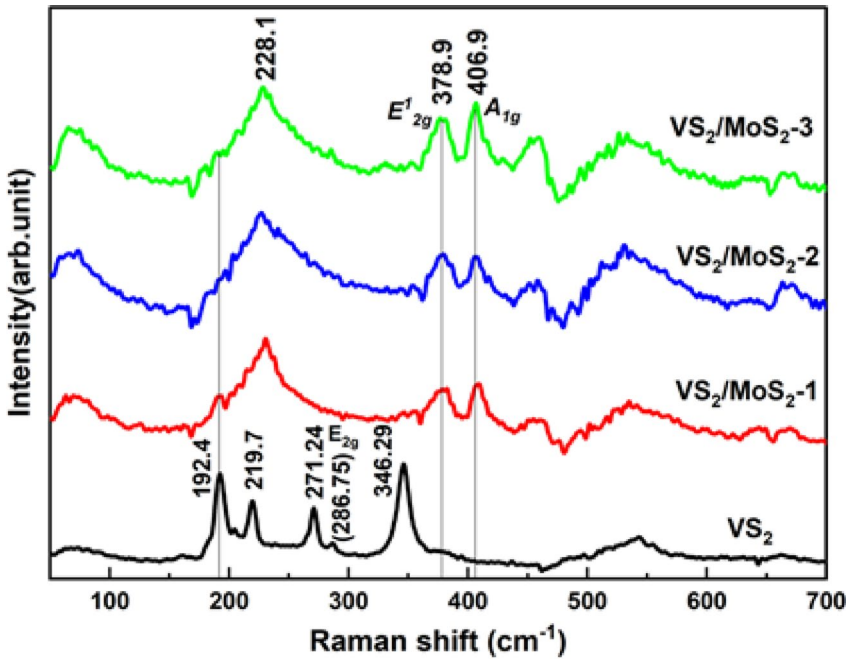

Fig. 2. Raman spectra of VS_2 and VS_2/MoS_2 nanocomposites.

element Vanadium. 2.293 keV is the L_α transition for molybdenum. The Sulfur peak at 2.307 keV is due to the K_α transition.

TEM analysis

Figure 5 represents the TEM images of VS_2/MoS_2-3 with different magnifications, which clearly show the nanosheets stacked together, forming a flower-shaped structure. The other two TEM images are shown in Figure S3. Figure 5c-e shows the HRTEM images with different scales and distinct crystallographic planes. (002) and (103) are the planes corresponding to MoS_2, with lattice spacing of d = 6.3 Å and d = 2.21 Å, respectively. (101) plane corresponds to VS_2, which confirms the inter-planar spacing of 2.51 Å. It matches well with the XRD data, conforming to the hexagonal phase of both VS_2 and MoS_2. Figure 5f is the SAED pattern confirming the presence of both VS_2 and MoS_2. Each circular ring present demonstrates the (002), (004), (100), and (102) planes corresponding to MoS_2 and VS_2, respectively. It shows the polycrystalline nature of the prepared sample.

XPS analysis

XPS is widely recognized as a powerful tool for surface analysis. It enables the identification of a material's surface elemental composition, oxidation states, and bonding environments, offering precise insights into the outermost layers, generally within the top ~ 10 nm of the sample. This data further confirms the presence of S, V, and Mo in the prepared sample. The comparison between pure VS_2 spectra and VS_2/MoS_2 spectra will give proof of nanocomposite formation. The XPS spectra of pristine VS_2 and VS_2/MoS_2 nanocomposite are presented in Fig. 6.a. The characteristic core levels for VS_2 are located at 524.7 eV and 517.4 eV. The V-$2p_{1/2}$ and V- $2p_{3/2}$ atomic orbitals correspond to the V^{4+} state. V^{2+} oxidation state is also present, confirmed by the peak located at 514 eV (Fig.S4(a))[46]. Due to the overexposure of the sample to air, another characteristic peak located at 530.1 eV is present due to O1s atomic orbital. The 162.8 eV and 163. 9 eV peaks are for S-$2p_{3/2}$ and S-$2p_{1/2}$ atomic orbitals, respectively, with the state S^{2-} Fig. S4(b)[57].

Figure 6a. presents the comparison between the XPS survey spectra of VS_2 and the VS_2/MoS_2-3 nanocomposite, while Fig. 6b and c display the high-resolution spectra of the V 2p and S 2p orbitals, respectively. In nanocomposite, the peaks for V-2p are slightly shifted towards the lower binding energy value as 524.5 and 517.04 eV that correspond to V-$2p_{1/2}$ and V-$2p_{3/2}$ with the same oxidation state V^{4+}[57]. The peak for state V^{2+} is not present here. The sulfur peak for 2p atomic orbital also shifted towards the lower binding energy value. S-$2p_{1/2}$ and S-$2p_{3/2}$ atomic orbitals correspond to binding energy values 163.22 and 162.08 eV, respectively, for S^{2-} state. Figure 6. d confirms the presence of Mo with the characteristic peak at 232.4 eV and 229.29 eV with the emission of electrons from the $3d_{3/2}$ and $3d_{5/2}$ atomic orbitals, and the Oxidation state is Mo^{4+}. A small peak at 226.45 eV is for the S-2s orbital[33]. The peak at 235.75 eV indicates the formation of the Mo^{6+} state[58]. The BE of nanocomposite is also less than that of pure MoS_2[36]. This peak shift is due to the transfer of electrons from the VS_2 to the MoS_2. The shift amount for both v-2p and S-2p is shown in Fig. 6b and c, respectively. This is the effect of the low work function of VS_2, the observed peak shifts indicate electron transfer from VS_2 to MoS_2, in conjunction with the strong interfacial coupling between the two materials[48]. There is no need for carbon correction because the peak for C-C is exactly at 284.6 eV, fig. S5(C). Individual XPS spectra and high-resolution XPS spectra are shown in Fig. S4 and Fig. S5.

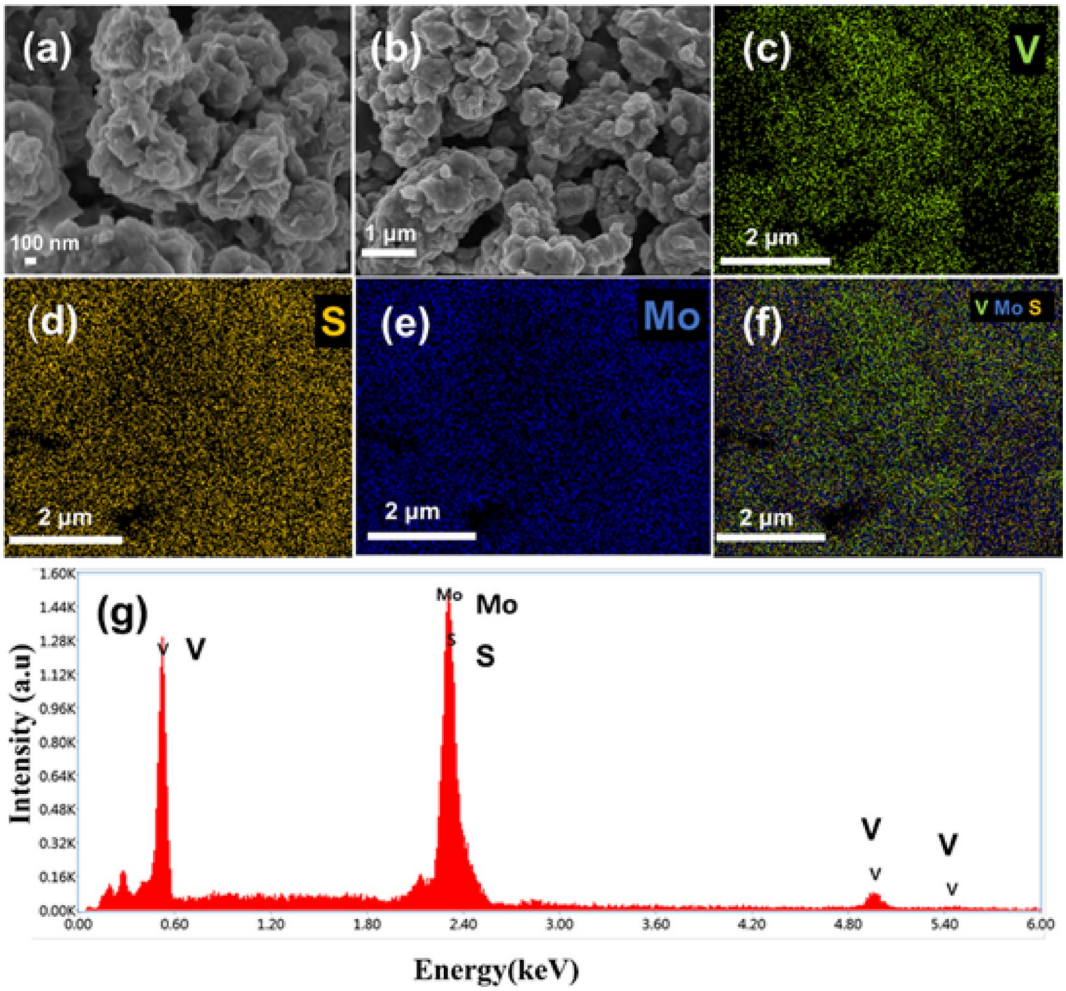

Fig. 3. (**a**, **b**) FESEM images at 100 nm and 1 µm scale; corresponding elemental maps of (**c**) V, (**d**) S, (**e**) Mo, (**f**) overall map, and (**g**) EDX spectra of VS_2/MoS_2-1 sample.

The atomic percentage can be calculated for the area under different oxidation states of the different elements present in a sample. The S-2p area is more in the VS_2/MoS_2-3 composite as compared to VS_2. Same for the S-2p oxidation states. The atomic percentage for each oxidation state is provided in the supporting information Table S2 and Table S3 for VS_2 and VS_2/MoS_2-3 composite. The oxidation states identified by XPS directly correlate with the antibacterial performance, indicating that the surface oxidation states govern the generation of reactive species responsible for bacterial inhibition. It is reported in a journal that Vanadium serves as the primary catalytic site for peroxymonosulfate (PMS) activation, where the generation of reactive oxygen species(ROS) originates from the redox transition among V^{5+}, V^{4+}, and V^{3+}.XPS analysis confirmed the V^{4+}/V^{5+} redox cycling, which plays a decisive role in radical generation and thereby enables efficient degradation of organic pollutants in the VS_4/PMS system[59].Nano-VO_x films have been shown to display strong antibacterial activity, particularly against S.aureus, with the effect intensifying at higher vanadium oxidation states due to enhanced intracellular ROS generation[60].Upon ultrasound stimulation, VS_4 generated abundant electrons that were efficiently captured by Mxene, resulting in enhanced electron-hole separation. This process promoted the production of multiple ROS species and imparted strong antibacterial activity, particularly through the POD-like catalytic generation of -OH by VS_4[61].Mo@ZIF-8 nanozymes, synthesized by refluxing Na_2MoO_4 with ZIF-8 and pyrolyzing at 600 °C, exhibited peroxidase-like •OH generation with broad antibacterial activity against *E. coli* and *S. aureus*, demonstrating strong potential as biocompatible antibacterial agents[62]. Thus, the oxidation states V^{4+} and Mo^{4+} identified by XPS play a crucial role in generating reactive species, which in turn enhance the inhibition of bacterial growth against E.coli, and S.aureus.

Optical study

A straightforward technique for determining the optical characteristics of the powdered crystalline materials is demonstrated using diffuse reflectance spectra (DRS). The energy gap between the valence band and the conduction band, where electrons can move, is referred to as the band gap[63]. Diffuse reflection is the phenomenon that arises from the reflection, refraction, diffraction, and absorption of particles oriented in all directions[64]. Kubelka-Munk theory is valid at the condition where the particle size is equivalent to or lower

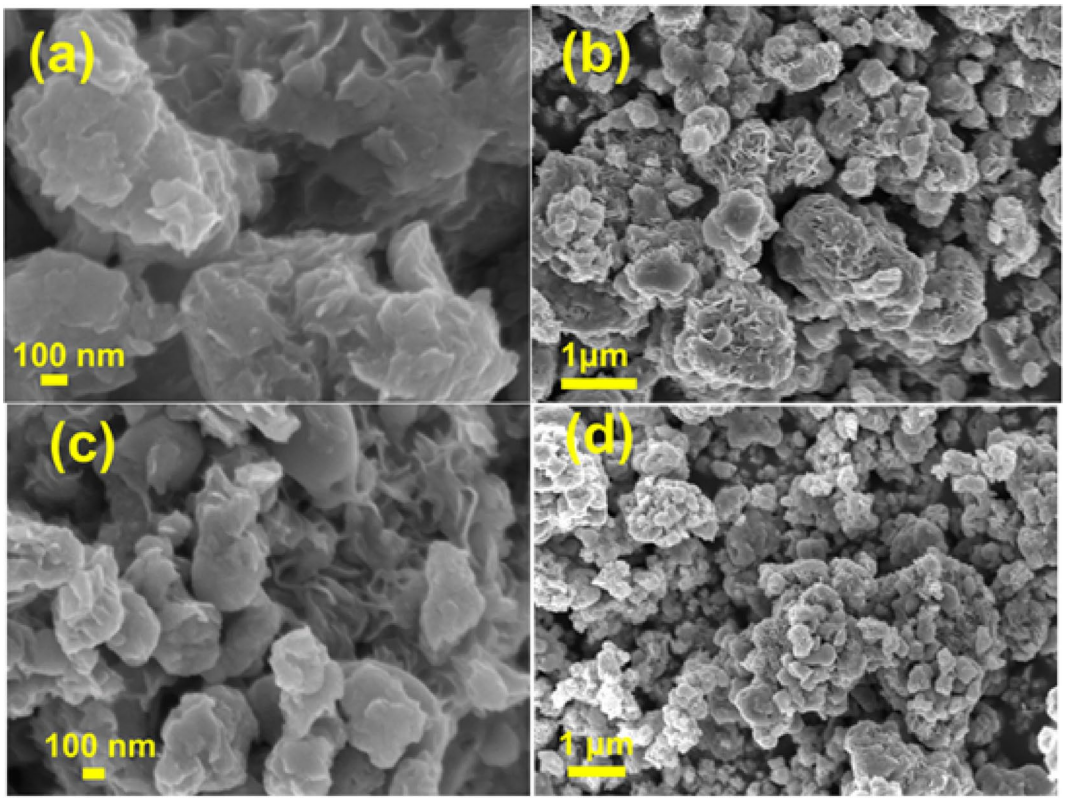

Fig. 4. FESEM images of (**a**, **b**) VS_2/MoS_2-2, (**c**, **d**) VS_2/MoS_2-3 at two different magnifications.

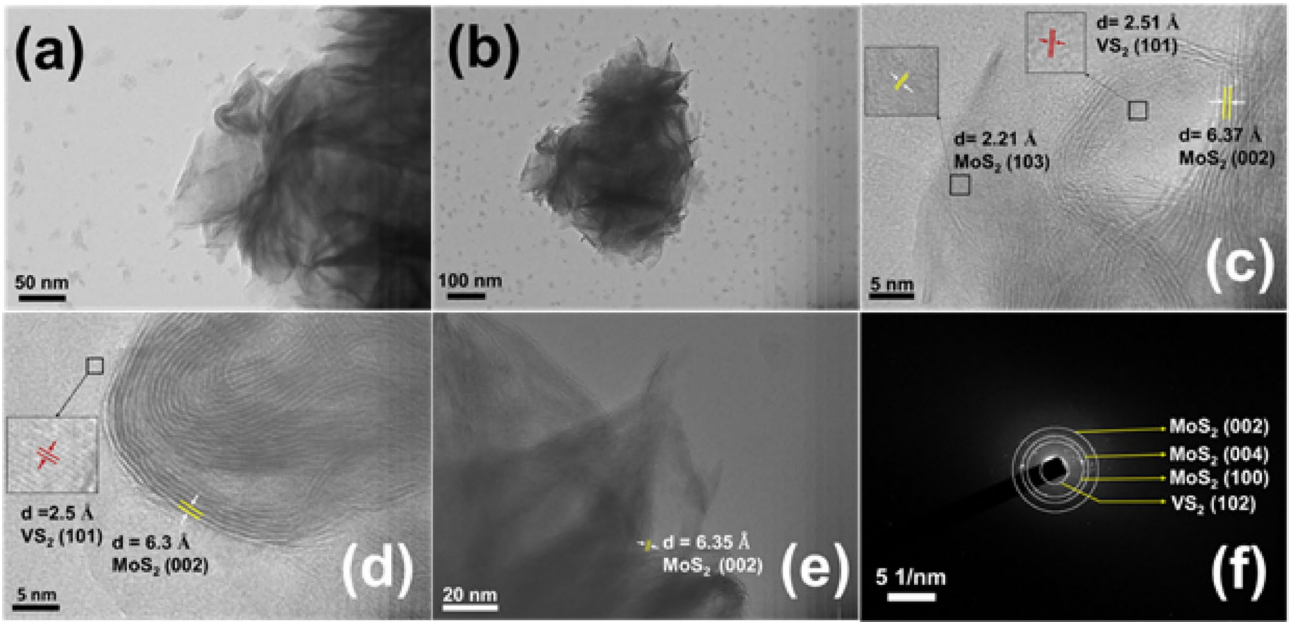

Fig. 5. (**a**, **b**) TEM images at various magnifications; corresponding (**c**–**e**) HRTEM images of VS_2/MoS_2-3 (**f**) SAED pattern.

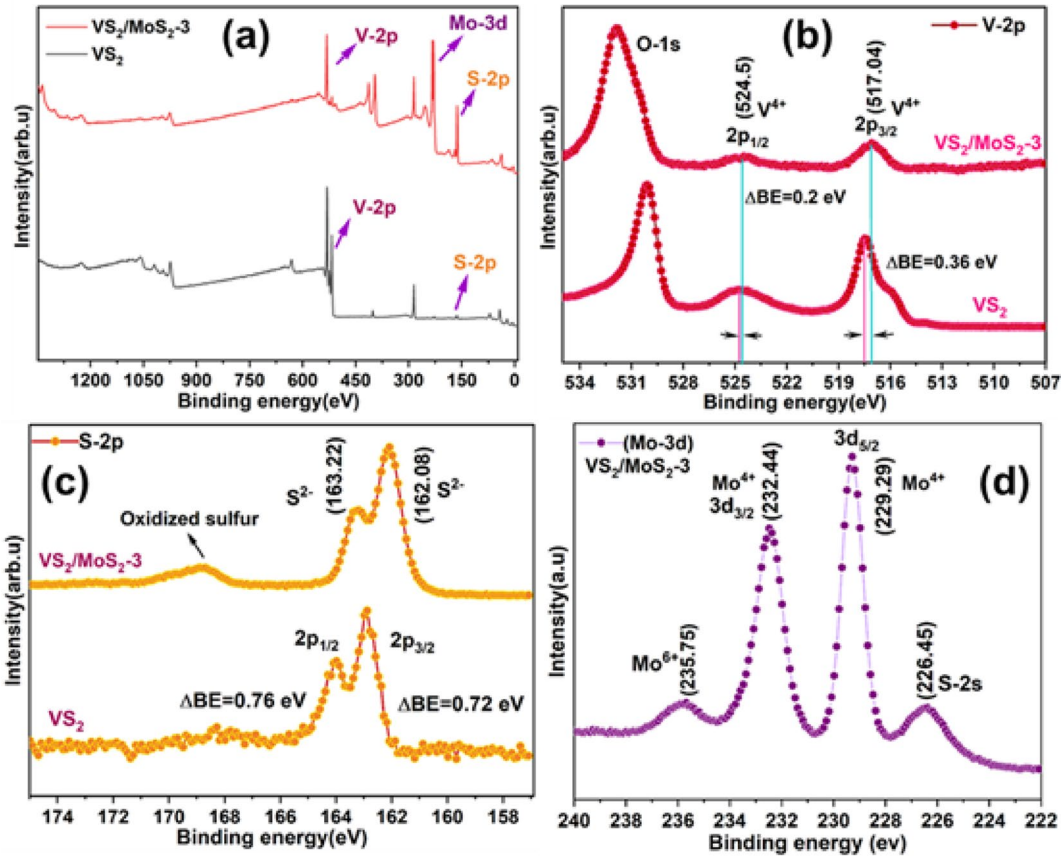

Fig. 6. (**a**) VS_2 and VS_2/MoS_2-3 XPS survey spectra: (**b**) V-2p, (**c**) S-2p, and (**d**) Mo-3d core level peaks.

than the wavelength of the incident ray. Figure 7(a) represents the reflectance plot of the samples. The sample's thickness does not affect reflectance when it falls within the appropriate range. The Kubelka-Munk is written for any wavelength as[65].

$$\frac{K}{S} = \frac{(1 - R_\infty)^2}{2R_\infty} = \mathrm{F}\,(\mathrm{R}\infty) \tag{4}$$

Here, R_∞ is the diffuse reflectance, and $f(R_\infty)$ is the Kubelka-Munk function. K as the absorption coefficient and S as the scattering coefficient. Absorption coefficient (α) and band gap (E_g) are related by the famous Tauc relation[63]. given by

$$\alpha h\nu = \mathrm{C}\ (h\nu - \mathrm{E_g})^{\mathrm{d}} \tag{5}$$

Here, the value of C is significantly influenced by transition probability. At the same time, 'ν' is the frequency of the incident light, and 'h' represents the Planck constant. Here, 'm' is related to the transition mode power factor. The 'd' value is different for various types of electronic transition, like d= ½ or 2 for direct and indirect allowed transitions. The absorption coefficient becomes twice for the perfect diffuse scattering of incident radiation. At this condition, scattering coefficient "s" remains constant with wavelength. Applying Eq. (5) for direct allowed transition, it can be written as[64,65]

$$[\mathrm{F}(\mathrm{R}_\infty)h\nu]^2 = \ \mathrm{A}\ (h\nu - \mathrm{E_g}) \tag{6}$$

Now E_g calculation was done by plotting $[F(R_\infty)h\nu]^2$ vs. hν. The evaluated values are listed in Table 2.

Figure 7.b confirms that the band gap of the prepared sample is increasing with an increased amount of molybdenum concentration. The energy gap and refractive index are two key parameters that determine semiconductors' optical and electrical behavior. The photon absorption threshold of the energy gap is determined by a semiconductor, while the transparency of the incident photon is measured by the refractive index[66]. The refractive index of materials can be evaluated through different approaches, including spectroscopic ellipsometry[67], prism coupling[68], refractometry[69], and UV-is spectroscopy. Among these, spectroscopic ellipsometry is generally regarded as the most precise and widely accepted method for thin films and smooth bulk substrates, as it yields both the real and imaginary components of the refractive index with high accuracy.

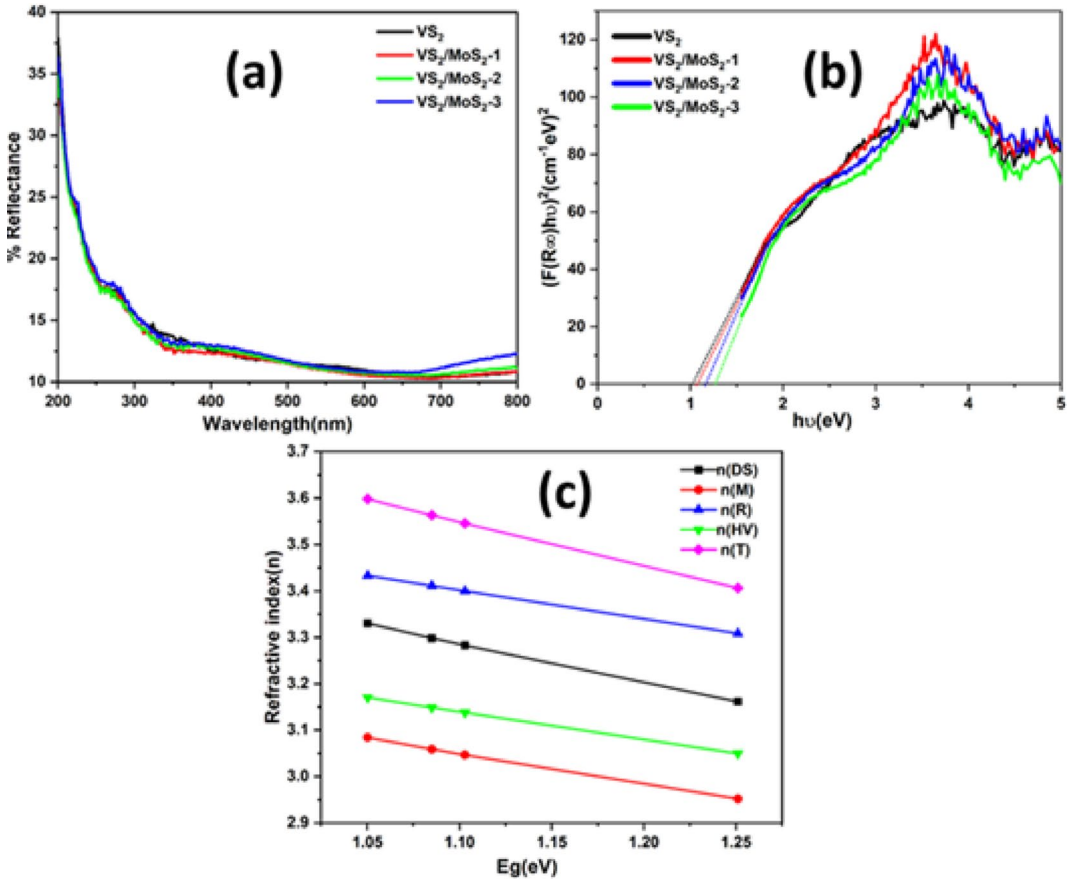

Fig. 7. (**a**) Reflectance spectra, (**b**) $[F(R_\infty)h\nu]^2$ vs. hν plot, (**c**) Variation of theoretically calculated n with E_g of VS_2 and VS_2/MoS_2 nanocomposites.

Evaluated optical data	VS_2	VS_2/MoS_2 -1	VS_2/MoS_2 -2	VS_2/MoS_2 -3
(E_g) (eV)	1.05 ± 0.001	1.08 ± 0.003	1.10 ± 0.002	1.25 ± 0.001
n_{DS}	3.30	3.29	3.28	3.16
n_M	3.08	3.05	3.04	2.95
n_R	3.43	3.41	3.40	3.30
n_{HV}	3.17	3.14	3.13	3.04
n_T	3.59	3.56	3.54	3.40

Table 2. Estimated optical parameter of the VS_2 and VS_2/MoS_2 composites.

Nevertheless, this technique cannot be applied to powdered samples, since their surface irregularities and intense diffuse scattering hinder reliable polarization-based measurements.

For the hydrothermally synthesized VS_2/MoS_2 nanocomposite obtained in powder form, UV-Vis diffuse reflectance spectroscopy(DRS) serves as the most appropriate technique. The reflectance spectra can be converted into the Kubelka-Munk function, and in combination with Tauc analysis, the optical bandgap can be estimated. Using this bandgap, the refractive index may be approximated through an empirical relation such as the Dimitrov-Sakka or Herve-Vandamme models. Although these estimates are indirect and less accurate compared to ellipsometry, they remain suitable for nanocomposite powders, where DRS provides the most dependable means of optical characterization. Therefore, while ellipsometry stands as the reference method for flat films and bulk samples, DRS-based evaluation offers the most credible pathway for refractive index determination in the present composite system. There are many theories for calculating the refractive index; some of the methods are listed below. According to the Moss relation[70], the refractive index (n) and energy gap (E_g) are related by the Eq.

$$E_g\, n_M^4 = K$$
$$n_M = \sqrt[4]{\frac{95}{E_g}} \tag{7}$$

Here, the K value is 95 eV. The Moss relation is valid within the 0.5 to 3.67 eV energy range. Another well-known relation is Ravindra's relation[71]

$$n_R = 4.084 - [0.62 * \mathrm{Eg}], \tag{8}$$

where the 'n' and 'E_g' are linearly connected. This model deals with the band gap energy 1.50 eV < E_g<3.50 eV. Using oscillator theory, Herve and Vandamme developed a relation between band gap and UV resonance energy, which gives the materials a low optical energy gap[72]. The model works between the energy range 2.00 eV < E_g<4.00 eV. It is the redefined Moss rule that is suitable for low optical energy gap materials. It is expressed as:

$$n^2 = 1 + \left(\frac{A}{E_g + B}\right)^2 \tag{9}$$

The value of A = 13.6 eV and B = 3.74 eV, with A representing the hydrogen ionization energy. This equation is expressed by:

$$n_{[H\nu]} = \sqrt{1 + \left(\frac{13.6}{E_g + 3.47}\right)^2} \tag{10}$$

Tripathy also put forth a different 'n' and 'E_g' relationship, where he showed that the 'n' and 'E_g' are exponentially related[73]

$$n_T = 1.73 \times [1 + 1.9017 \times e^{-0.539 \times E_g}] \tag{11}$$

Another way of calculating the band gap is the Dimitrov and Sakka relation[74], given by the Eq.

$$\frac{{n_{DS}}^2 - 1}{{n_{DS}}^2 + 2} = 1 - \sqrt{\frac{E_g}{20}} \tag{12}$$

The calculated values of the refractive index are listed in Table 2. The refractive index value in the higher wavelength region is higher than in the lower wavelength region, as seen in Fig. 7 c[72,75,76]. The blue shift in the absorption spectra increases the band gap of the material from VS_2 to higher concentrations of molybdenum gradually. This is due to the quantum confinement effect[77]. This is also confirmed from the XRD data that the crystallite size of the prepared material gradually decreases with a higher amount of molybdenum concentration. The prepared material can be used in solar cells, photodetectors, and waveguides, as it has a lower band gap calculated from DRS data due to the high refractive index[78].

Antimicrobial properties

The procured result showed that there is a sequential reduction in turbidity of both gram-negative and gram-positive bacterial strains with an increase in the concentration of the test material, which is shown in the Figs. 8 and 9 respectively. There is a visible turbidity bacterial culture incubated along with DMF, which suggests that DMF is not meddlesome in bacterial growth. This implies that the test material can significantly inhibit the growth of both gram-positive and gram-negative bacteria.

The result obtained from the disk diffusion method showed that the material has a significant antibacterial property against both gram-negative (*E. coli*) and gram-positive (*S. aureus*) bacteria. The inhibition zone diameter obtained against E. coli and S. aureus is 12 mm and 11 mm, respectively. It shows that the inhibition zone against E. coli is more prominent than S. aureus, which implies that the material has better antibacterial efficacy against gram-negative bacteria than gram-positive bacteria. The disk diffusion method also shows that the material is easily diffused over the agar plate to inhibit the growth of bacteria. Figure 10. illustrates the evaluation of antimicrobial properties of the material in both gram-negative and gram-positive strains, the related inhibition zone against (a) S. aureus, (ATCC 25923), (b) E. coli, (ATCC 25922), whereas 1 & 3 are positive control impregnated disks with DMF, and 2, 4 are disks impregnated with material dissolved in DMF.

In this manuscript, the primary method selected was the broth dilution method to evaluate the antibacterial efficacy of the material against both gram-negative (ATCC-25922, E. coli) and gram-positive (ATCC-25923, S. aureus) bacteria. In this particular method, three different concentrations of material were taken to evaluate which concentration has better efficacy against both, where all the concentrations that were taken are effective, significantly inhibiting the growth. For further confirmation of the antibacterial activity of the synthesized MoS_2/VS_2 nanocomposite, the disk diffusion method was adopted. In this process, a sterile disk was impregnated with material and then applied to a bacterial culture to observe the sensitivity of the bacteria towards the nanocomposite.

There are several methods being used for the antibacterial assay, such as flow cytometry, ATP bioluminescence assay, and time kill assay, which is better for real-time monitoring, but here we selected the broth dilution and disk

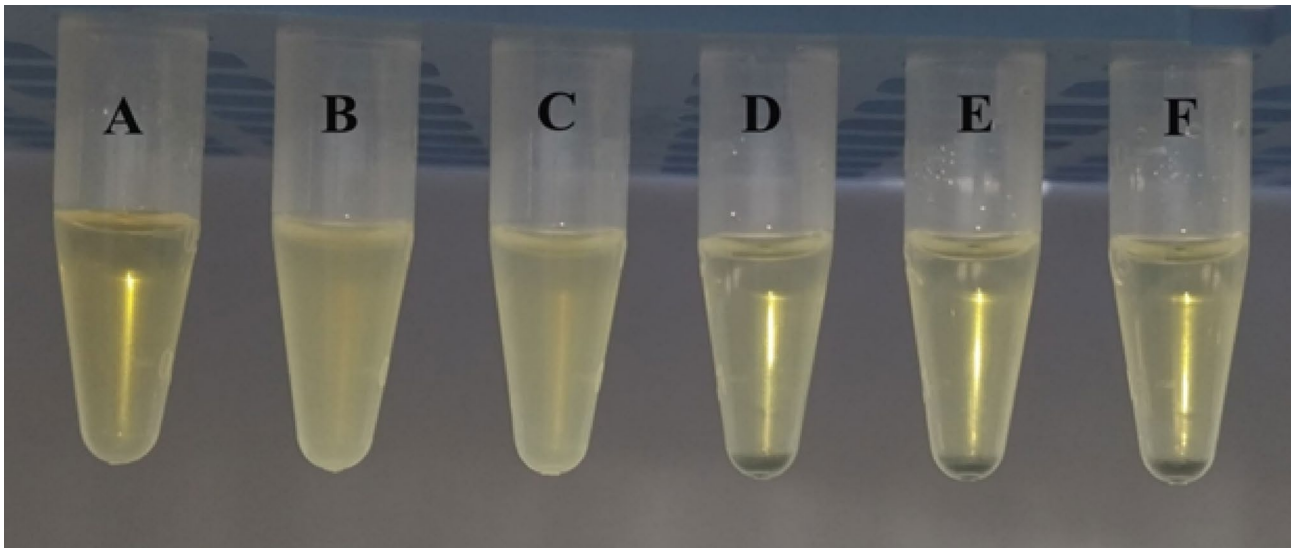

Fig. 8. Evaluation of MIC of material against gram-negative bacterial strain (E. coli) (**A**) Negative control, (**B**) positive control, (**C**) bacterial culture along with DMF (**D**–**F**) bacterial strain along with the test material at different concentration i.e. 25 mg/mL, 50 mg/mL, 100 mg/mL respectively.

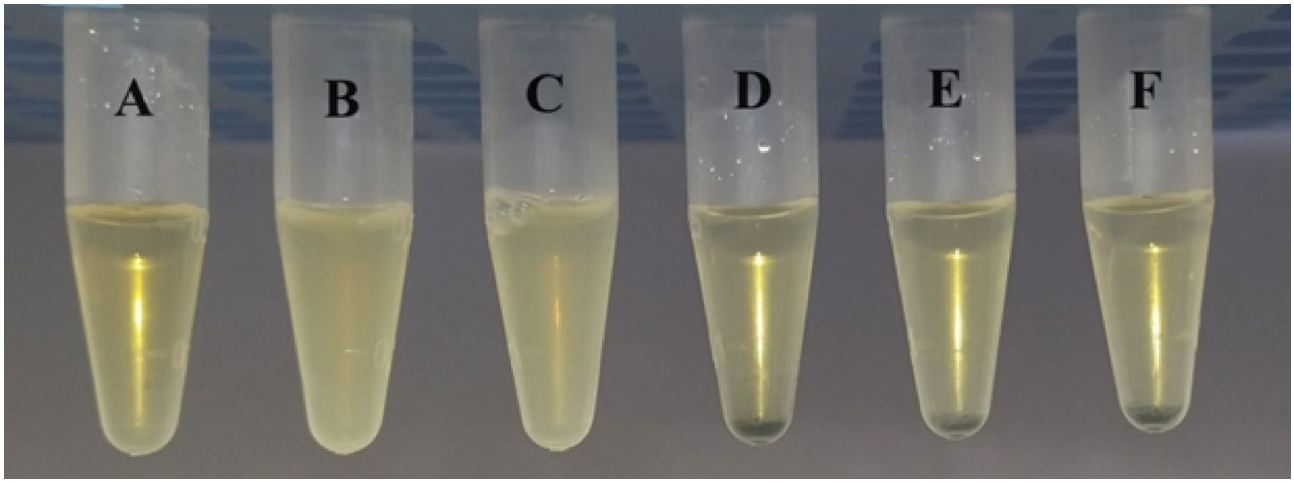

Fig. 9. Evaluation of MIC of material against gram-positive bacterial strain (S. aureus) (**A**) Negative control, (**B**) positive control, (**C**) bacterial culture along with DMF (**D**–**F**) bacterial strain along with the test material at different concentrations i.e. 25 mg/mL, 50 mg/mL, 100 mg/mL, respectively.

diffusion method for their broad acceptability. These are conventional antibacterial assays for initial screening of antibacterial efficacy in a microbiology laboratory. The diffusion capacity of MoS_2/VS_2-3 nanocomposite and its sensitivity towards bacteria were well observed in the disk diffusion method. In this study, MoS_2/VS_2-3 nanocomposite has been used as the sole material for antibacterial assay; therefore, the comparison focused on the effect of the material on gram-negative and gram-positive bacteria rather than different samples.

Conclusion

The experimental data revealed the formation of VS_2/MoS_2 nanocomposite by hydrothermal synthesis. The hexagonal phases of both VS_2 and VS_2/MoS_2 were identified from the XRD analysis, with decreased crystallite size from 4.6 to 4.29 with the increased Mo concentration. The micro strain increased from 36.77 to 38.09 with an increase in Mo content for VS_2/MoS_2 nanocomposites. The surface morphology revealed the flower-like structure for VS_2/MoS_2 with a high surface area and a nanosheet-like structure for VS_2. Raman spectroscopy identified the vibrational modes of V-S and Mo-S bonds. The bandgap value increased from 1.08 eV to 1.25 eV, and the refractive index decreased from 3.29 to 3.16 with an increase in Mo content as revealed in the optical study. The XPS peak shift is due to the transfer of electrons from VS_2 to MoS_2. The various oxidation states of the elements were identified from the XPS data. The antimicrobial activity analyzed through the disk diffusion

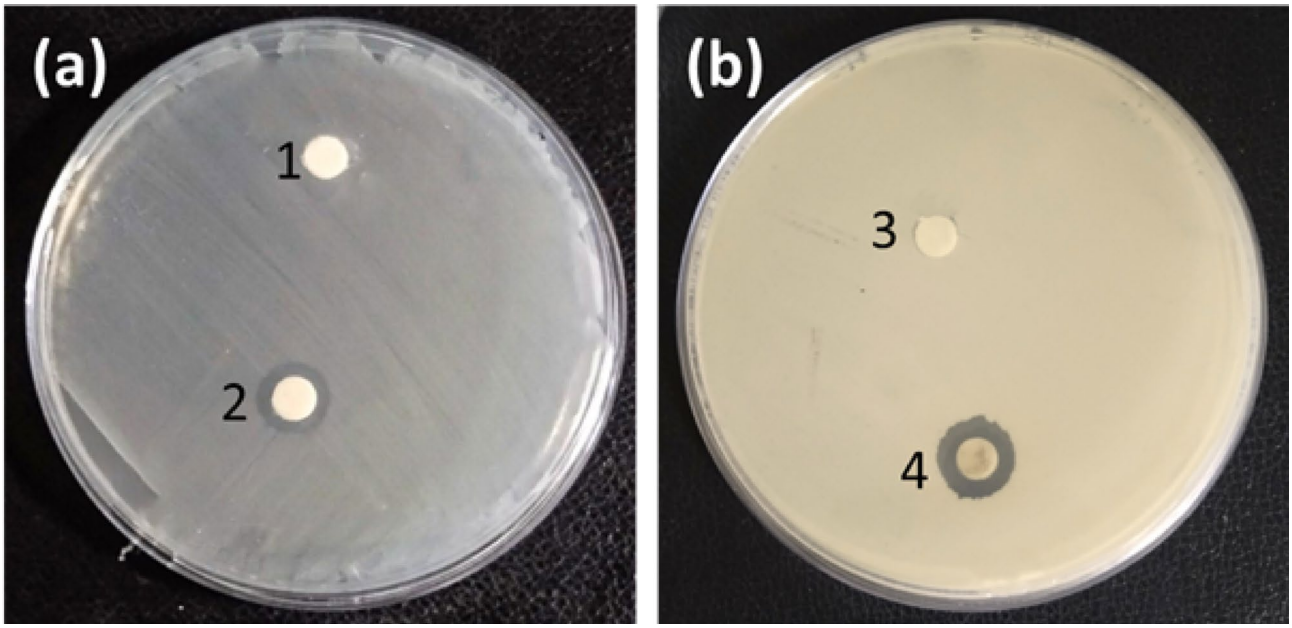

Fig. 10. Evaluation of antimicrobial properties of the material in both gram-positive and gram-negative strains, the related inhibition zone against (**a**) S. aureus, (ATCC 25923), (**b**) E. coli, (ATCC 25922), whereas 1 & 3 are positive control impregnated disks with DMF, and 2 & 4 are disks impregnated with material dissolved in DMF.

method on gram-positive and gram-negative bacteria revealed the superior performance of gram-negative bacteria with better efficacy over gram-positive ones. Such antimicrobial findings are suitable for various biological applications as well.

Data availability

The datasets used and/or analysed during the current study are available from the corresponding author on reasonable request.

Received: 13 July 2025; Accepted: 17 September 2025
Published online: 22 October 2025

References

1. Li, W., Kheimeh Sari, H. M. & Li, X. Emerging layered metallic vanadium disulfide for rechargeable Metal-Ion batteries: progress and opportunities. *ChemSusChem* **13**, 1172–1202 (2020).
2. Zhao, W. & Ding, F. Energetics and kinetics of phase transition between a 2H and a 1T MoS 2 monolayer—a theoretical study. *Nanoscale* **9** (6), 2301–2309 (2017).
3. Huang, Q., Shen, J., Lu, Y., Ye, R. & Gong, S. Insights into the structural evolution of MoS2 from the semiconductive 2H to metallic 1T phase. *J. Phys. Chem. C.* **127** (35), 17406–17414 (2023).
4. Sahoo, D., Senapati, S. & Naik, R. Progress and prospects of 2D VS2 transition metal dichalcogenides. *FlatChem* **36**, 100455 (2022).
5. Xu, H. et al. High responsivity and gate tunable Graphene-MoS2 hybrid phototransistor. *Small* **10**, 2300–2306 (2014).
6. Aftab, S. & Hegazy, H. H. Emerging trends in 2D TMDs photodetectors and Piezo-Phototronic devices. *Small* **19**, 2205778 (2023).
7. Vikraman, D. et al. Assembling highly efficient X-ray and UV-visible light detectors using a VS 2 –MoS 2 and VS 2 –WS 2 hybrid composite-embedded perovskite layer. *J. Mater. Chem. A.* **12**, 14769–14785 (2024).
8. An, Y. et al. Multifunctional lateral Transition-Metal disulfides heterojunctions. *Adv. Funct. Mater.* **30**, 2002939 (2020).
9. Li, X. et al. A self-powered graphene–MoS2 hybrid phototransistor with fast response rate and high on–off ratio. *Carbon* **92**, 126–132 (2015).
10. Voshell, A., Terrones, M. & Rana, M. Thermal and photo sensing capabilities of Mono- and Few-Layer Thick transition metal dichalcogenides. *Micromachines* **11**, 693 (2020).
11. Das, M. et al. An Atomically Thin and Photosensitive Vanadium Disulfide Memtransistor. Preprint at (2023). https://doi.org/10.21203/rs.3.rs-2558699/v1
12. Agarwal, V. & Chatterjee, K. Recent advances in the field of transition metal dichalcogenides for biomedical applications. *Nanoscale* **10**, 16365–16397 (2018).
13. Lu, C., Liu, Y., Ying, Y. & Liu, J. Comparison of MoS2, WS2, and graphene oxide for DNA adsorption and sensing. *Langmuir* **33**, 630–637 (2017).
14. Kou, Z. et al. A promising gene delivery system developed from pegylated MoS2 nanosheets for gene therapy. *Nanoscale Res. Lett.* **9**, 587 (2014).
15. Liu, C. et al. Rapid water disinfection using vertically aligned MoS2 nanofilms and visible light. *Nat. Nanotechnol.* **11**, 1098–1104 (2016).
16. Han, Q. et al. CpG loaded MoS 2 nanosheets as multifunctional agents for photothermal enhanced cancer immunotherapy. *Nanoscale* **9**, 5927–5934 (2017).
17. Yin, W. et al. High-Throughput synthesis of Single-Layer MoS2 nanosheets as a Near-Infrared Photothermal-Triggered drug delivery for effective cancer therapy. *ACS Nano*. **8**, 6922–6933 (2014).

18. Cheng, L. et al. PEGylated WS2 nanosheets as a multifunctional theranostic agent for in vivo Dual-Modal CT/Photoacoustic imaging guided photothermal therapy. *Adv. Mater.* **26**, 1886–1893 (2014).
19. Yang, X. et al. Antibacterial activity of two-dimensional MoS 2 sheets. *Nanoscale* **6**, 10126–10133 (2014).
20. Huang, X. W. et al. Silk fibroin-assisted exfoliation and functionalization of transition metal dichalcogenide nanosheets for antibacterial wound dressings. *Nanoscale* **9**, 17193–17198 (2017).
21. Kim, T. I., Kim, J., Park, I. J., Cho, K. O. & Choi, S. Y. Chemically exfoliated 1T-phase transition metal dichalcogenide nanosheets for transparent antibacterial applications. *2D Mater.* **6**, 025025 (2019).
22. Wang, T. et al. A two-step gas/liquid strategy for the production of N-doped defect-rich transition metal dichalcogenide nanosheets and their antibacterial applications. *Nanoscale* **12**, 8415–8424 (2020).
23. Bang, G. S. et al. DNA-Assisted exfoliation of tungsten dichalcogenides and their antibacterial effect. *ACS Appl. Mater. Interfaces.* **8**, 1943–1950 (2016).
24. Qumar, U. et al. Synergistic effect of Bi-doped exfoliated MoS 2 nanosheets on their bactericidal and dye degradation potential. *Dalton Trans.* **49**, 5362–5377 (2020).
25. Wei, F. et al. Recoverable peroxidase-like Fe3O4@MoS2-Ag nanozyme with enhanced antibacterial ability. *Chem. Eng. J.* **408**, 127240 (2021).
26. Ikram, M. et al. Promising performance of chemically exfoliated Zr-doped MoS 2 nanosheets for catalytic and antibacterial applications. *RSC Adv.* **10**, 20559–20571 (2020).
27. Liu, J., Cheng, W., Zhang, K. & Liu, H. Photoinduced Ce–MoS2/WO3 nanocomposites with enhanced photodynamic and enzyme-like activity for rapid sterilization. *Ceram. Int.* **49**, 17424–17436 (2023).
28. Alahmadi, M. et al. One-step hydrothermal synthesis of flower-like MoS2/VS2 nanocomposite for biomedical applications. *Inorg. Chem. Commun.* **157**, 111336 (2023).
29. Wang, J., Wang, Y., Zhang, D., Chen, C. & Yang, Z. CoS2/MoS2 nanosheets with enzymatic and photocatalytic properties for bacterial sterilization. *ACS Appl. Nano Mater.* **4**, 7698–7711 (2021).
30. Wu, R. et al. Membrane destruction and phospholipid extraction by using two-dimensional MoS 2 nanosheets. *Nanoscale* **10**, 20162–20170 (2018).
31. Li, Y. et al. Modification of a rod-shaped Bi-MOF with MoS2 nanosheets to form a p-n heterojunction for enhanced antimicrobial activity. *Appl. Surf. Sci.* **654**, 159434 (2024).
32. Kokilavani, S. et al. Integrating Ag2WO4 on VS4 nanoplates with synergy of plasmonic photocatalysis and boosted visible-light harvesting and its antibacterial applications. *J. Alloys Compd.* **865**, 158810 (2021).
33. Kasinathan, K. et al. Synthesis of biogenic chitosan-functionalized 2D layered MoS2 hybrid nanocomposite and its performance in pharmaceutical applications: In-vitro antibacterial and anticancer activity. *Int. J. Biol. Macromol.* **149**, 1019–1033 (2020).
34. Chen, X., Yu, K., Shen, Y., Feng, Y. & Zhu, Z. Synergistic effect of MoS2 nanosheets and VS2 for the hydrogen evolution reaction with enhanced humidity-sensing performance. *ACS Appl. Mater. Interfaces.* **9** (48), 42139–42148 (2017).
35. Koczkur, M., Mourdikoudis, K., Polavarapu, S., Skrabalak, E. & L. & Polyvinylpyrrolidone (PVP) in nanoparticle synthesis. *Dalton Trans.* **44**, 17883–17905 (2015).
36. Jadhav, V. S. et al. Studies on colloidal stability of PVP-coated LSMO nanoparticles for magnetic fluid hyperthermia. (2013). https://doi.org/10.1039/C3NJ00554B
37. Lu, G. et al. Imparting functionality to a metal–organic framework material by controlled nanoparticle encapsulation. *Nat. Chem.* **4**, 310–316 (2012).
38. Si, R., Zhang, Y. W., You, L. P. & Yan, C. H. Self-Organized monolayer of nanosized ceria colloids stabilized by Poly(vinylpyrrolidone). *J. Phys. Chem. B.* **110**, 5994–6000 (2006).
39. Zhang, W., Rosano-Ortega, G., Hu, Y., Bai, L. & Qin, L. New investigation in PVP-mediated synthesis of noble metallic nanomaterials. *J. Nanosci. Nanotechnol.* **12** (3), 2634–2639 (2012).
40. Shameli, K. et al. Investigation of antibacterial properties silver nanoparticles prepared via green method. *Chem. Cent. J.* **6**, 73 (2012).
41. Kottmann, A., Mejía, E., Hémery, T., Klein, J. & Kragl, U. Recent developments in the Preparation of silicones with antimicrobial properties. *Chem. – Asian J.* **12**, 1168–1179 (2017).
42. Gopal, J. et al. Assays evaluating antimicrobial activity of nanoparticles: A myth buster. *J. Clust Sci.* **29**, 207–213 (2018).
43. Kourmouli, A. et al. Can disc diffusion susceptibility tests assess the antimicrobial activity of engineered nanoparticles? *J. Nanoparticle Res.* **20**, 62 (2018).
44. Saxena, S. et al. Nanotechnology approaches for rapid detection and theranostics of antimicrobial resistant bacterial infections. *ACS Biomater. Sci.* **8** (6), 2232–2257 (2022).
45. Dos Santos Ramos, M. A. et al. Nanotechnology-based drug delivery systems for control of microbial biofilms: a review. *Int. J. Nanomed.* **13**, 1179–1213 (2018).
46. Ren, X., Wei, Q., Wu, F., Wang, Y. & Zhao, L. CNT/VS2-MoS2 with multi-interface structure for improved hydrogen evolution reaction. *Chem. Commun.* **57**, 2531–2534 (2021).
47. Du, C. et al. In situ engineering MoS2 NDs/VS2 lamellar heterostructure for enhanced electrocatalytic hydrogen evolution. *ACS Sustain. Chem. Eng.* **6**, 15471–15479 (2018).
48. Zhang, S., Wang, J., Torad, N. L., Xia, W., Aslam, M. A., Kaneti, Y. V., … Yamauchi,Y. Rational design of nanoporous MoS2/VS2 heteroarchitecture for ultrahigh performance ammonia sensors. Small, 16(12), 1901718(2020).
49. Holder, C. F. & Schaak, R. E. Tutorial on powder X-ray diffraction for characterizing nanoscale materials. *ACS Nano.* **13**, 7359–7365 (2019).
50. Das, S., Senapati, S., Pradhan, G. K., Varadharajanperumal, S. & Naik, R. A. Facile Microwave-Assisted Nanoflower-to-Nanosphere morphology tuning of CuSe1−xTe1 + x for optoelectronic and dielectric applications. *ACS Appl. Nano Mater.* **6**, 5298–5312 (2023).
51. N. Kottam, A. B., K.b. & C. S. Synthesis, characterization and supercapacitor electrode performances of VS2 nanosheets. *Mater. Today Proc.* **46**, 545–549 (2021).
52. Kumar, G. M. et al. Ultrathin VS2 nanodiscs for highly stable electro catalytic hydrogen evolution reaction. *Int. J. Energy Res.* **44**, 811–820 (2020).
53. Xu, R. et al. VS2 microflowers with in situ embedded Few-Layer MoS2 nanobelts for enhanced hydrogen evolution reaction at high current density. *J. Electrochem. Soc.* **167**, 026508 (2020).
54. He, P. et al. Layered VS_2 Nanosheet-Based aqueous Zn ion battery cathode. *Adv. Energy Mater.* **7**, 1601920 (2017).
55. Jiménez Sandoval, S., Yang, D., Frindt, R. F. & Irwin, J. C. Raman study and lattice dynamics of single molecular layers of ${\ mathrm{MoS}}_{2}$. *Phys. Rev. B.* **44**, 3955–3962 (1991).
56. Li, L. et al. Vanadium disulfide flakes with nanolayered titanium disulfide coating as cathode materials in lithium-ion batteries. *Nat. Commun.* **10**, 1764 (2019).
57. Shi, M. et al. A promising electrochemical sensor based on PVP-induced shape control of a hydrothermally synthesized layered structured vanadium disulfide for the sensitive detection of a sulfamethoxazole antibiotic. *Analyst* **149**, 386–394 (2024).
58. Hussain, S. et al. Large-area, continuous and high electrical performances of bilayer to few layers MoS2 fabricated by RF sputtering via post-deposition annealing method. *Sci. Rep.* **6**, 30791 (2016).
59. Zeng, Q. et al. Activity and mechanism of vanadium sulfide for organic contaminants oxidation with peroxymonosulfate. *J. Colloid Interface Sci.* **635**, 358–369 (2023).

60. Wang, J. et al. A functionalized surface modification with vanadium nanoparticles of various Valences against implant-associated bloodstream infection. *Int. J. Nanomed.* **12**, 3121–3136 (2017).
61. He, Y. et al. Bioactive VS4-based sonosensitizer for robust chemodynamic, sonodynamic and osteogenic therapy of infected bone defects. *J. Nanobiotechnol.* **22**, 31 (2024).
62. Lian, Z. et al. Mo@ZIF-8 nanozyme Preparation and its antibacterial property evaluation. *Front Chem* **10**, (2022).
63. Abdullahi, S. S. et al. Sımple method for the Determınatıon of band gap of a nanopowdered sample Usıng Kubelka Munk theory. *J Niger Assoc. Math. Phys* **35**, (2016).
64. Torrent, J. & Barrón, V. Diffuse reflectance spectroscopy. in Methods of Soil Analysis Part 5—Mineralogical Methods 367–385 (Wiley, Ltd, doi:https://doi.org/10.2136/sssabookser5.5.c13. (2008).
65. Supriya, S., Das, S., Senapati, S. & Naik, R. Cu2Te/CoTe nanoparticles with tuneable bandgaps: implications for photovoltaic and optoelectronic devices. *Surf. Interfac.* **44**, 103823 (2024).
66. Kumar, P. C., Mohapatra, A., Senapati, S., Pradhan, M. & Naik, R. A facile microwave-assisted synthesis of bismuth copper oxytelluride for optoelectronic and photodetection applications. *FlatChem* **42**, 100580 (2023).
67. Munkhbat, B., Wróbel, P., Antosiewicz, T. J. & Shegai, T. O. Optical constants of several multilayer transition metal dichalcogenides measured by spectroscopic ellipsometry in the 300–1700 Nm range: high Index, Anisotropy, and hyperbolicity. *ACS Photonics*. https://doi.org/10.1021/acsphotonics.2c00433 (2022).
68. Onodera, H., Awai, I. & Ikenoue, J. Refractive-index measurement of bulk materials: Prism coupling method. *Appl. Opt.* **22**, 1194–1197 (1983).
69. Onofri, F. Critical angle refractometry for simultaneous measurement of particles in flow: size and relative refractive index. *Part. Part. Syst. Charact.* **16**, 119–127 (1999).
70. Moss, T. S. A Relationship between the Refractive Index and the Infra-Red Threshold of Sensitivity for Photoconductors. *Proc. Phys. Soc. Sect. B* 63, 167 (1950).
71. Ravindra, N. M., Auluck, S. & Srivastava, V. K. On the Penn gap in semiconductors. *Phys. Status Solidi B*. **93**, K155–K160 (1979).
72. Hervé, P. & Vandamme, L. K. J. General relation between refractive index and energy gap in semiconductors. *Infrared Phys. Technol.* **35**, 609–615 (1994).
73. Tripathy, S. K. Refractive indices of semiconductors from energy gaps. *Opt. Mater.* **46**, 240–246 (2015).
74. Das, S., Senapati, S., Pradhan, G. K., Varadharajanperumal, S. & Naik, R. A facile microwave-assisted nanoflower-to-nanosphere morphology tuning of CuSe1−x Te1 + x for optoelectronic and dielectric applications. *ACS Appl. Nano Mater.* **6** (7), 5298–5312 (2023).
75. Parishani, M., Nadafan, M. & Malekfar, R. Effect of phase change in the layered VSx nanosheets for investigation of dielectric function and optical properties at the wavelength range of 10–20 µm. *J. Appl. Phys.*, **132**(15) (2022).
76. Parishani, M., Nadafan, M. & Malekfar, R. Z-scan investigation to evaluate the third-order nonlinear optical properties of cauliflower-like VS_2 structures. *JOSA B*. **38**, 1586–1592 (2021).
77. Wang, W. et al. Self-assembled MoS 2 /rGO nanocomposites with tunable UV-IR absorption. *RSC Adv.* **8**, 2410–2417 (2018).
78. Parida, A., Senapati, S., Samal, S., Bisoyi, S. & Naik, R. One-Pot hydrothermal synthesis of SnMnS nanosheets for dielectric energy storage applications. *ACS Appl. Nano Mater.* **6**, 11230–11241 (2023).

Acknowledgements

The author, Dr. R. Naik, acknowledges the central instrument facility of ICT-IOC for different characterization and DST-SERB, Govt of India. The authors also thank the Indian Council of Medical Research-Regional Medical Research Centre, Bhubaneswar, for providing a scientific platform.

Author contributions

B. Dandasena: Writing – original draft; Formal analysis; Methodology; Data curation; Resources S. Das: Data curation; MethodologyA.Parida: Data curation, MethodologyR. Praharaj: Investigation; Data curationS. Samal: Data curation; Methodology; Formal analysisC. Sripan: Data curation, MethodologyR. Naik: Writing – review & editing; Supervision; Conceptualization; Visualization.

Funding

There is no funding for this research work.

Declarations

Competing interests

The authors declare no competing interests.

Additional information

Supplementary Information The online version contains supplementary material available at https://doi.org/10.1038/s41598-025-20959-x.

Correspondence and requests for materials should be addressed to R.N.